

Precise local functionalization of covalent organic framework for efficient carrier separation in photocatalytic H₂ evolution



Lei Hao^{a,1}, Rongchen Shen^{a,1}, Guijie Liang^{b,*}, Mengmeng Kang^c, Can Huang^a, Peng Zhang^d, Xin Li^{a,*}

^a Institute of Biomass Engineering, Key Laboratory of Energy Plants Resource and Utilization, Ministry of Agriculture and Rural Affairs, South China Agricultural University, Guangzhou 510642, China

^b Hubei Key Lab Low Dimens Optoelect Mat & Devices, Hubei University of Arts and Science Xiangyang 441053, China

^c School of Materials Science and Engineering, Henan Normal University, No. 46, East of Construction Road, Xinxiang, Henan Province 453007, China

^d State Centre for International Cooperation on Designer Low-Carbon & Environmental Materials (CDLCEM), School of Materials Science and Engineering, Zhengzhou University, Zhengzhou, Henan 450001, China

ARTICLE INFO

Keywords:

Covalent organic frameworks
Photocatalytic hydrogen evolution
Fluorenone
Local structure regulation
Carrier separation

ABSTRACT

Improving carrier transport rate and suppressing carrier recombination are two huge challenges in the photocatalytic applications of covalent organic frameworks (COFs)-based semiconductors. In this study, we propose a strategy to enhance carrier transport efficiency by regulating the local microenvironment of the electronic characteristics in the acceptors through structural modification. Three different functional group-modified fluorenone-based COFs were successfully synthesized through precise design. The results demonstrate that the photocatalytic hydrogen evolution activities of COFs modified with electron-donating functional groups are significantly higher than that of COFs modified by electron-withdrawing functional groups. Specifically, the photocatalytic hydrogen evolution performance of phenyl-modified FOOPh-COF could reach 228.5 mmol h⁻¹ g⁻¹, which is 11.8 times higher than that of Br atom-modified FOOBr-COF (19.3 mmol h⁻¹ g⁻¹). Femtosecond time-resolved transient absorption spectroscopy (fs-TAS) results reveal that introducing phenyl groups into the acceptor significantly enhances its inhibitory effect on the carrier recombination. Density functional theory calculations further prove that modifying the acceptor by electron-donating functional groups can achieve the increased electron density in the C=O active center. The electrons in the C=O region in the phenyl-modified fluorenone structure are more enriched and delocalized, which can enhance the speed of electron migration, shorten the migration distance, and inhibit carrier recombination. After loading Pt, it has the lowest H^{*} adsorption-free energy among three samples. This work clarifies the importance of the functionalization modification of COFs' acceptors in regulating the local electronic environment and further provides new insights into the structure-activity relationship of fluorenone-based COF-based photocatalysts.

1. Introduction

The use of semiconductors in green hydrogen production from photocatalytic water splitting has proven to be a prominent research area in the sustainable energy fields. To this end, various kinds of semiconductor photocatalysts, such as metal oxides, sulfides [1] and nitrides, metal free materials [2–4] and their heterojunctions [5–10], as well as cocatalysts [11,12], have been extensively exploited and applied in the field of photocatalytic hydrogen production. Among all these available photocatalysts, covalent organic frameworks (COFs)-based

semiconductors have garnered significant attention in photocatalysis over the past ten years due to their excellent physical and chemical properties [13–17]. However, serious carrier recombination and low electron mobility are the main factors hindering the development of COFs-based photocatalysts [18,19]. Thus, different strategies have been developed to boost the charge separation and photocatalytic activity of COFs-based photocatalysts [17]. Apart from constructing COF-based heterojunctions, it remains challenging to rationally design novel COFs or regulate the local microenvironment of COFs-based semiconductors to achieve the maximum charge separation and utilization

* Corresponding authors.

E-mail addresses: guijie-liang@hbus.edu.cn (G. Liang), xinli@scau.edu.cn (X. Li).

¹ These authors contributed equally to this work.

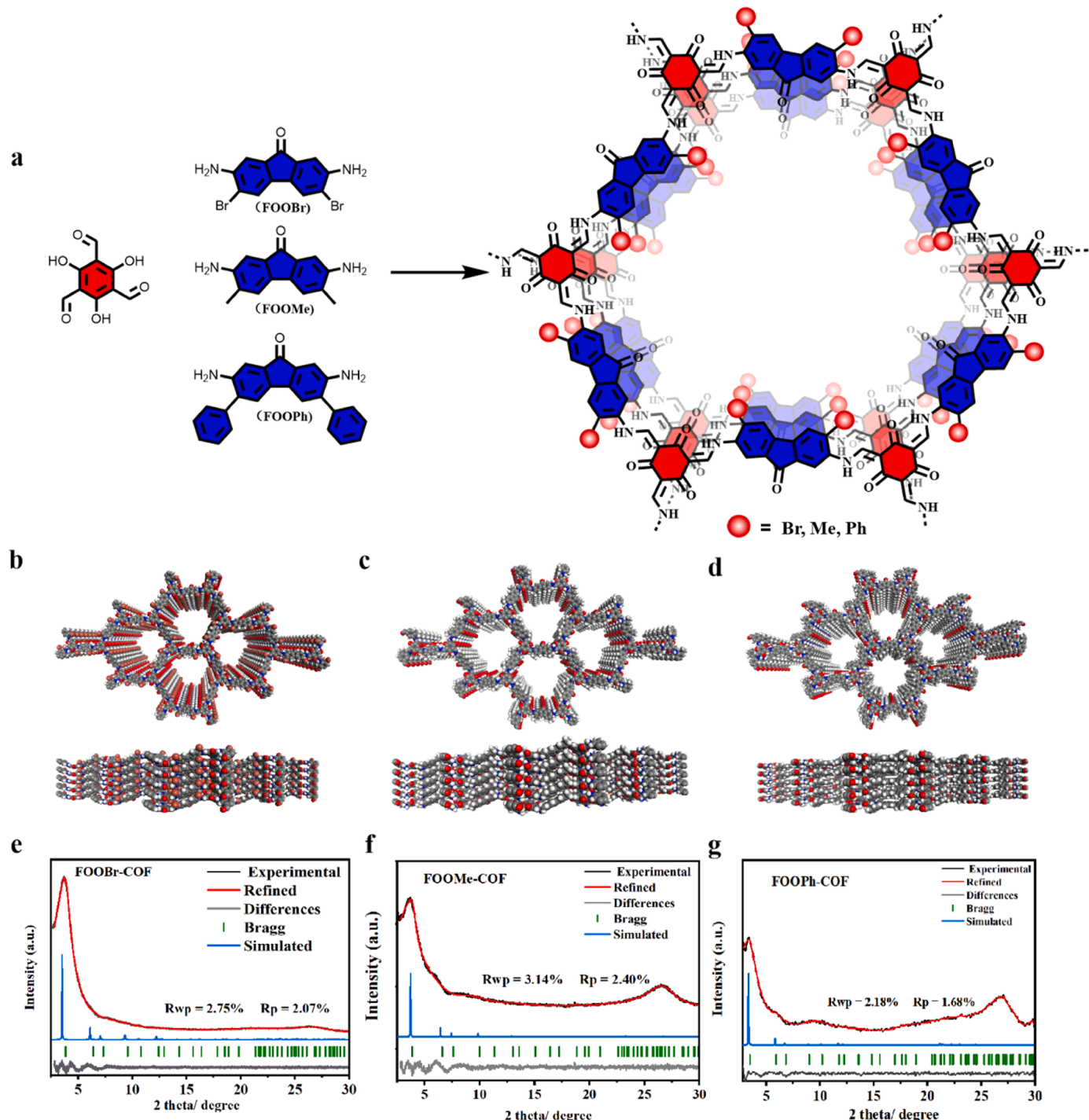


Fig. 1. Design and synthesis of three structurally functionalized COFs. a) The scheme for synthesizing FOO(X)-COFs. b) – d) Crystal structures of FOOBr-COF, FOOME-COF and FOOPh-COF. Structural models for FOOBr-COF, FOOME-COF and FOOPh-COF with perfectly eclipsed AA stacking patterns. e) – g) Experimental and simulated PXRD patterns of FOOBr-COF ($R_p=2.07\%$, $R_{wp}=2.75\%$), FOOME-COF ($R_p=2.40\%$, $R_{wp}=3.14\%$), FOOPh-COF ($R_p=1.68\%$, $R_{wp}=2.18\%$).

for the high-efficiency photocatalysis.

Typically, regulating the local microenvironment of COFs-based semiconductors could be achieved by several approaches, including reconstructing positional and framework isomers [20,21], introducing the metal or non-metal atoms [22,23], tailoring surface groups [24, 25] and forming surface single-molecular junctions [26]. Frankly speaking, all these microenvironment regulation strategies can energetically strengthen the favorable donor-acceptor (D-A) effects in COFs, thus improving the charge-carrier separation in COFs-based photocatalysts [27]. In other words, enhancing the strong push-pull effect in

the D-A structure can further enable the creation of a robust built-in electric field, which is favorable to the positive migration of more electrons and thus weaken the unexpected charge recombination. Thereby, the facilitated transfer kinetics of photogenerated charges driven by strengthening D-A effects will effectively expedite the directional migration and spatial separation of carriers for highly efficient photocatalysis [28–32]. On the one hand, to further enhance the electron traction ability of acceptors, modifying the acceptor structure with halogens [33] or cyanide groups [24] has been found to significantly improve carrier-separation efficiency. On the other hand, choosing the

donor modules with stronger electron supply capabilities [34] or modifying the carrier transport channels between D-A [35] can also accelerate charge separation and improve photocatalytic performance. However, to date, the direct modification of acceptor in D-A COFs using electron-donating functional groups has seldom been reported. Specifically, for the acceptor in D-A COF systems that contain potential active sites, effectively controlling charge behavior in electron-enriched regions to refine charge transfer pathways remains a huge challenge [36]. Moreover, precise micro-local electronic regulation is a simple yet effective strategy to deeply understanding the underling photocatalytic mechanisms [25]. It can also fundamentally avoid the charge recombination or loss caused by long-distance electron transfer in D-A structures. Accordingly, it should be interesting and challenging to finely tailor the microenvironment of local electron-rich centers by precise local functionalization of acceptor, which may provide a new focus on systematically revealing the electric charge kinetics, catalytic mechanism and structure–property relationship of COFs-based photocatalysts.

Herein, we propose the new strategy for directly regulating the carrier transport behavior of electron-rich active centers in electron acceptors by modifying the acceptor module with electron-donating functional groups (Fig. 1). This strategy can significantly shorten the charge transfer distance and improve the carrier separation efficiency [37–39]. Notably, COFs modified with electron-donating functional groups exhibit better photocatalytic performance than that modified with electron-withdrawing functional groups. Moreover, the detailed photocatalytic mechanisms were further analyzed by combining the theoretical and experimental studies. This work provides new insights into the modification strategy of D-A COF in photocatalysis, which regulates the microenvironment of local electron-rich centers by modifying acceptor modules in COF, thereby improving charge transfer efficiency and deeply elucidating its mechanism of action.

2. Experimental section

2.1. Chemicals and materials

All chemicals and reagents were of analytical grade materials and used as received without further purification. The 4,4'-dimethylbenzophenone (98%), 3,6-dibromo-9-fluorenone (96%), phenylpinacolborane, Pd(PPh_3)₂Cl₂, Pd(OAc)₂, SnCl₂, TFA (CF₃COOH) were all supplied by Energy Chemicals. The 1,4-dioxane was purchased from Macklin Chemicals. Tp (2,4,6-Triformylphloroglucinol, 97%) was supplied by Jilin Chinese Academy of Sciences-Yanshen Technology Co. Ltd. The *o*-DCB (1,2-dichlorobenzene, 99%), anhydrous *n*-BuOH (*n*-Butanol, 99.4%), pyrrolidine (Py, 98%), ascorbic acid (>99.0%) were purchased from Macklin Chemicals.

2.2. Synthesis of FOOBr-COF, FOOME-COF and FOOPh-COF

A Pyrex tube was charged with 2,4,6-trihydroxybenzene-1,3,5-tricarbaldehyde (0.08 mmol), functionalized 2,7-diamino-9H-fluorene-9-one-7-diamino-9H-fluorene-9-one (0.12 mmol), *o*- 1,2-dichlorobenzene (0.75 mL), *n*-BuOH (0.25 mL), and Py (0.1 mL). This mixture was homogenized by sonication for 10 minutes and the tube was then flash frozen at 77 K (liquid N₂ bath) and degassed by three freeze-pump-thaw cycles and evacuated to an internal pressure of 100 m Torr. The tube was sealed off and then heated at 120 °C for 3 days. The brown precipitate was collected by centrifugation and washed with tetrahydrofuran (100 mL) and anhydrous acetone (200 mL). After drying at 120 °C, the product was obtained as a black-red powder. (The synthesis method of functionalized 2,7-diamino-9H-fluorene-9-one can be found in the supporting information.).

2.3. Photocatalytic hydrogen evolution

The photocatalytic water splitting reaction under visible-light

irradiation was performed in a 120 mL three necked glass flask under frontal irradiation. In a typical process, 2 mg (3 wt% Pt) of the photocatalyst was dispersed in a three necked glass flask with 100 mL 0.1 M ascorbic acid (AA) aqueous solution. The air in the three necked glass flask was replaced with N₂ and sealed, and then irradiated with a 350 W Xe lamp (PLS-SXE300, Beijing Perfect Light Technology Co., Ltd, $\lambda > 420$ nm). During the photocatalytic reaction, the suspension was continuously stirred. The generated hydrogen was detected by GC-9500 online chromatograph.(AQE= 2 $M/N_p \times 100\%$, where M is the amount of hydrogen molecules and N_p represents the incident photons.)[40].

2.4. Catalysts characterization

N₂ sorption measurements were performed on a volumetric sorption instrument (Autosorb-iQ-MP). Prior to the gas sorption studies of COFs, the samples were dried under a dynamic vacuum (<10–3 Torr) at room temperature (RT) followed by heating to 120 °C for 12 h. Using the N₂ adsorption isotherms, the surface areas were calculated over a pressure range 0.01–0.9 =P/P₀ using Brunauer-Emmett-Teller (BET). Fourier transformed infrared (FTIR) spectra were tested on a Nicolet Avatar 6700 FT-IR spectrometer (Thermo Fisher, America). The UV-vis diffuse reflection spectra (UV-vis DRS) of the pristine FOOBr-COF, FOOME-COF, FOOPh-COF powders were carried out on a Shimadzu UV-2550 UV-vis-NIR spectrophotometer. X-ray photoelectron spectroscopy (XPS) data was carried out by a VG ESCALAB250 surface measurement system. The specific condition is that the excitation source: Al K α Ray ($h\nu = 1486.6$ eV), Beam spot: 400um, vacuum degree of the analysis chamber is better than 5.0 E-7 mBar, working voltage: 12 kV, filament current: 6 mA, full spectrum scanning: pass energy: 100 eV, step size: 1 eV; narrow spectrum scanning: the energy is 50 eV, and the step size is 0.1 eV. The narrow spectrum shall be subject to at least 5 times of cyclic signal accumulation (different scanning times for different elements), and the binding energy correction: charge correction shall be conducted with C 1 s = 284.80 eV binding energy as the energy standard. Transmission electron microscopy (TEM) images were obtained with a JEOL JEM-2010 electron microscope. Scanning electron microscopy (SEM) was conducted on a Hitachi S-4800 field emission scanning electron microscope. (Detailed characterization of transient absorption spectra can be found in supporting confidence).

2.5. Computational models

All calculations were performed using Guassian 09 software package. According to density functional theory (DFT), the geometric optimization of the FOOBr-COF, FOOME-COF, FOOPh-COF cross sections were performed at the B3LYP/6-311 g (d, p) level. The calculation results of the molecular electrostatic potential (ESP) are obtained by Guassian 09 software. The Generalized Gradient Approximation within the Density Function Theory (DFT) is implemented in this study as provided by the module DMol3. All geometry optimization calculations are performed using the Becke–Lee–Yang–Parr (BLYP) exchange correlation functional and the double numerical with polarization (DNP) basis set since it is the best set available in DMol3. The charge density difference map was constructed by the Multiwfn program and Visual Molecular Dynamics (VMD). (For detailed information, please refer to the supporting information).

3. Results and discussion

3.1. Catalyst synthesis and structural characterization

First, three types of COFs were synthesized through the Schiff base reaction between 1,3,5-triformyl phloroglucinol (Tp) and amino fluorenones modified with three functional groups under the solvothermal condition catalyzed by acetic acid, namely FOOBr-COF, FOOME-COF, and FOOPh-COF (Fig. 1a) [41]. A series of characterizations were

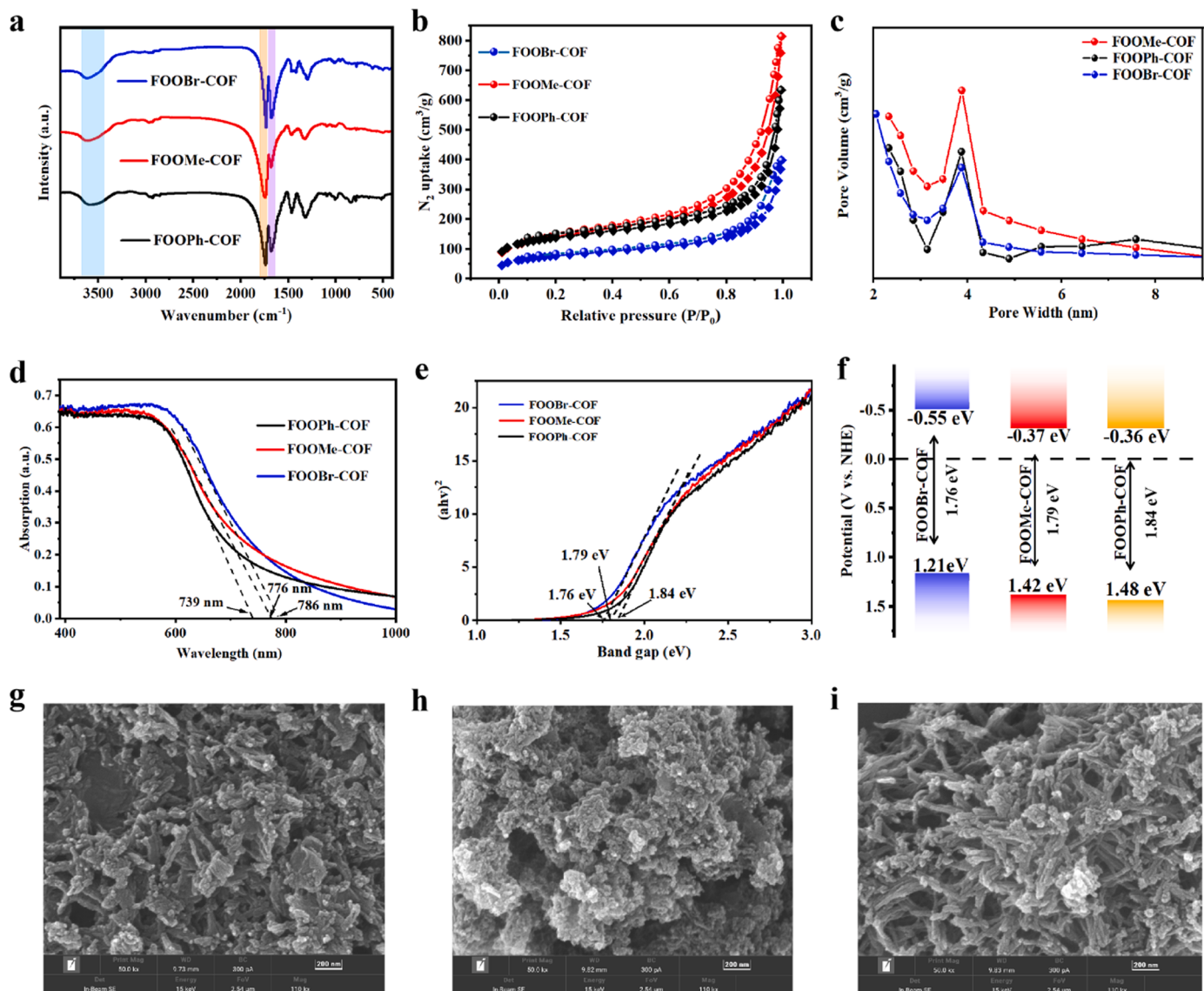


Fig. 2. The structure information of FOOBr-COF, FOOMe-COF and FOOPh-COF. a) FT-IR spectrum of FOOBr-COF, FOOMe-COF and FOOPh-COF. b) The nitrogen adsorption (solid) and desorption (open) isotherms for FOOBr-COF, FOOMe-COF and FOOPh-COF. c) Pore size distribution of FOOBr-COF, FOOMe-COF and FOOPh-COF. d) UV-vis absorption spectra of FOOBr-COF, FOOMe-COF and FOOPh-COF. e) Bandgap of FOOBr-COF, FOOMe-COF and FOOPh-COF. f) Energy band positions of FOO(X)-COFs. g), h) and i) are SEM images of FOOBr-COF, FOOMe-COF, and FOOPh COF.

performed to verify the chemical structure and properties of these COFs. Powder X-ray diffraction (PXRD) analysis was conducted to determine the crystallinity of FOOBr-COF, FOOMe-COF, and FOOPh-COF (Fig. 1b-g). The PXRD pattern of FOOBr-COF exhibits a strong peak at 3.7° , which can be attributed to the (100) plane. Slight peaks at 6.3° and 26.8° are also observed. Similarly, the PXRD pattern of FOOMe-COF displays three diffraction peaks at 3.7° , 6.5° , and 26.8° , corresponding to the (100), (110), and (001) planes, respectively. Additionally, the primary diffraction peaks of FOOPh-COF at 3.2° , 5.9° , and 26.5° are identified as reflections from the (100), (110), and (001) planes. These results are consistent with the theoretical predictions of the AA interlayer stacking model (Figure S1). Then, the stability of the crystallinity was assessed, and it was observed that the material maintained good crystallinity even after 6 hours in 1 M NaOH and 1 M HCl solutions (Figure S2).

The FTIR spectrum of the synthesized COFs indicate the absence of peaks corresponding to N-H stretching (3300 cm^{-1}) and aldehyde stretching (1633 cm^{-1}), suggesting a condensation reaction between amines and aldehydes. Furthermore, a prominent peak at approximately

$\sim 1725\text{ cm}^{-1}$ was observed, which is attributed to the cyclohexanone structure resulting from enol-ketone tautomerism (Figs. 2a and S3). The permanent porosity of FOOBr-COF, FOOMe-COF, and FOOPh-COF was studied by N_2 adsorption/desorption isotherm at 77 K (Fig. 2b)[42,43]. The results demonstrate that all three COFs exhibit the rapidly increased adsorption of N_2 at low pressures ($P/P_0 < 0.05$), indicating a type II adsorption isotherm. The Brunauer Emmett Teller (BET) specific surface areas of three COFs were determined to be 375 (FOOBr-COF), 695 (FOOMe-COF), and $632\text{ m}^2\text{ g}^{-1}$ (FOOPh-COF), respectively. The pore size distribution, as determined by the nonlocal density functional theory (DFT) model (Fig. 2c), was found to be 3.8 nm . The high-resolution N 1 s X-ray photoelectrochemical (XPS) spectra of three types of COFs show only one core binding energy peak at 399.7 eV , corresponding to the C-N group. In their O 1 s XPS spectra, the binding energy peak at 530.5 eV belongs to C=O, while the binding energy peak of C-OH belongs to $\sim 531.0\text{ eV}$. The peak with binding energy of 533.5 eV belongs to the oxygen species adsorbed by the as-prepared material. In the C 1 s XPS spectrum, the core energy level peaks at 284.7 , 286.2 , and $\sim 288.0\text{ eV}$ correspond to C=C, N-C, and C=O bonds, respectively

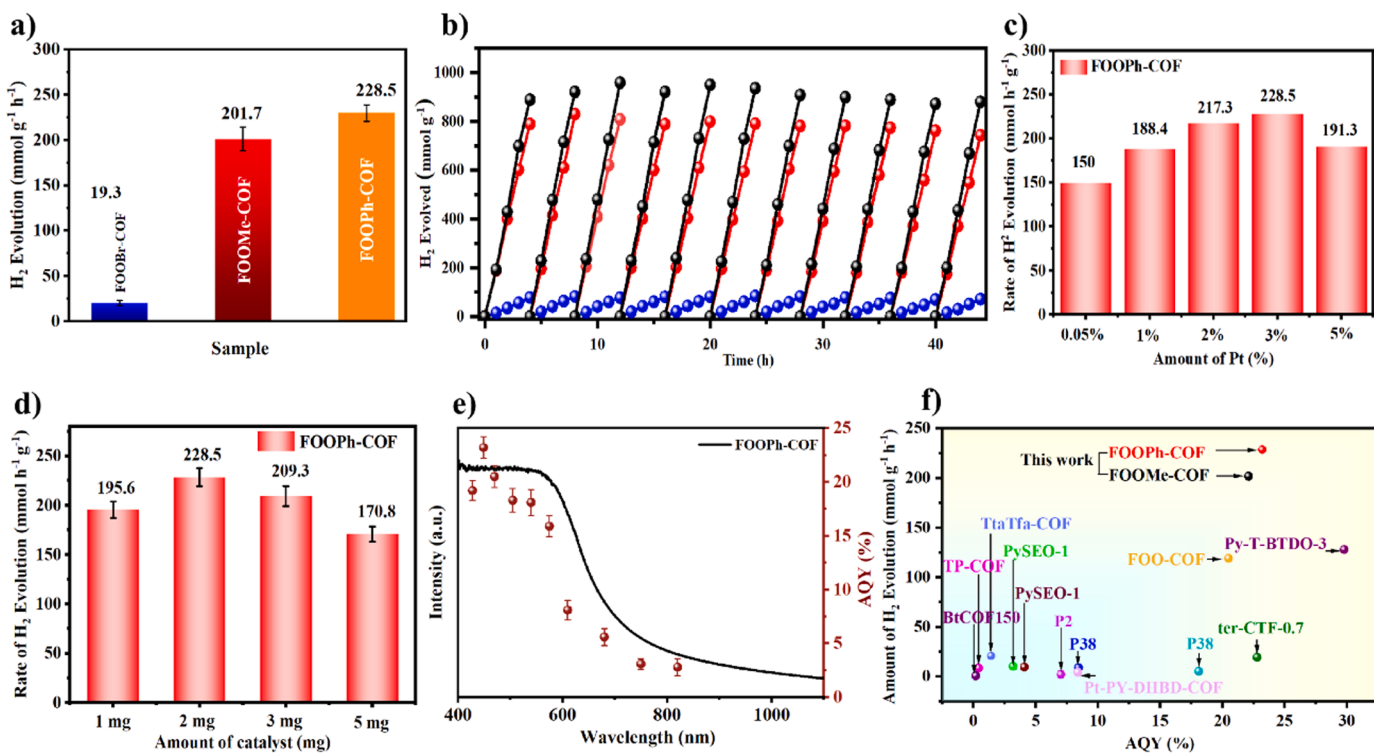


Fig. 3. Photocatalytic performance. a) Photocatalytic performance of FOO(X)-COFs. b) Photocatalytic durability test of FOOPh-COF. c) Hydrogen production rates with different amounts of cocatalyst (Pt) (2 mg catalyst, 0.1 M AA, 80 mL water) (FOOPh-COF). d) Hydrogen production rate of different amounts of photocatalysts (3% Pt, 0.1 M AA, 80 mL water) (FOOPh-COF). e) Wavelength-dependent AQE of photocatalytic H_2 production for FOOPh-COF. f) Comparison of COF-based semiconductor photocatalytic hydrogen evolution performance.

(Figure S5-S7). In addition, the in-situ XPS test results were basically unchanged (Figure S8). The different carbon environments in COFs were studied through solid-state ^{13}C NMR spectroscopy[44]. As shown in Figure S9, the peak at around 191 ppm belongs to the carbonyl group in the fluorenone structure. The signal at around 184 ppm is a cyclohexanone-type carbonyl carbon ($\text{C}=\text{O}$) characteristic. In addition, the peaks at around 147, 135, and 121 ppm confirm the presence of C-N and C=C bonds in the COFs linked to ketene amine. Specifically, FOOMe-COF exhibits a peak at around 20 ppm, corresponding to the characteristic methyl peak. Additionally, for FOOPh-COF, the peaks in the aromatic region are significantly enhanced, indicating the successful introduction of the benzene ring. This further verifies the correctness of three COF's structures. Furthermore, the electronic structures of three COFs were analyzed using UV-Vis and VB-XPS. Fig. 2d shows that the absorption range of three COFs extends to a wide range of wavelengths, up to 730–790 nm. The optical band gaps (E_g) of FOOBr-COF, FOOMe-COF, and FOOPh-COF were determined to be 1.76, 1.79, and 1.84 eV, respectively (Fig. 2e) [45]. As seen in the VB-XPS plots (Figure S4), the conduction band (CB) levels of FOOBr-COF, FOOMe-COF, and FOOPh-COF are -0.55 , -0.37 , and -0.36 eV, respectively, indicating that they are thermodynamically capable of driving the photocatalytic water splitting. Additionally, the morphology of the as-prepared COFs was studied by scanning electron microscopy (SEM) and transmission electron microscopy (TEM). As shown in Figs. 2g-i and S10, all three types of COFs exhibit dendritic interlacing morphology, which could be related to their good hydrophilicity. The water contact angle also confirms this point. Hydrophilicity tests were conducted on three types of COFs, as shown in Figure S11. Their contact angles were 75.6° (FOOBr-COF), 76.1° (FOOMe-COF), and 45.3° (FOOPh-COF), respectively, indicating that they all have good hydrophilicity.

3.2. Photocatalytic hydrogen evolution performance

The photocatalytic performance of the as-prepared COFs (2 mg) was tested under visible light irradiation, with Pt (3 wt%) as cocatalysts and ascorbic acid (0.1 M, 80 mL) as a sacrificial agent. All three types of COFs exhibit excellent photocatalytic hydrogen evolution rates[22]. FOOPh-COF and FOOMe-COF display excellent photocatalytic hydrogen evolution rates up to 228.5 and 201.7 $\text{mmol h}^{-1} \text{g}^{-1}$, respectively. In contrast, the photocatalytic hydrogen evolution ability of FOOBr-COF, after electron-withdrawing halogen atom bromine modification, decreases to only 19.3 $\text{mmol h}^{-1} \text{g}^{-1}$ (Fig. 3a). All the as-prepared COFs show good stability during the photocatalytic reaction (Fig. 3b)[23,46]. No obvious decrease could be found during the 44 hours of the hydrogen evolution reaction. Additionally, we separately investigated the relationship between the amount of catalyst (or cocatalyst) and hydrogen evolution performance of FOOPh-COF(Fig. 3c and d)[47]. The results show that the amount of cocatalyst is not linearly related to the photocatalytic activity due to the light shielding effect. The optimum conditions for the photocatalytic hydrogen evolution reaction were determined to be 3 wt% cocatalysts, 2 mg usage of catalysts, and 0.1 M sacrificial agent. We also tested and compared the effects of different types of sacrificial agents on the photocatalytic performance of FOOPh-COF and found that an acidic sacrificial agent is crucial for improving the photocatalytic hydrogen evolution performance of this type of COF. When the sacrificial agents are TEOA and Na_2SO_3 , the photocatalytic hydrogen evolution performance of FOOPh-COF decreases to 2.4 and 0.6 $\text{mmol g}^{-1} \text{h}^{-1}$ (Figure S12). This result may be related to the protonation of such COFs under acidic sacrificial agent conditions. The wavelength-dependent photocatalytic performance of FOOPh-COF was quantified by using apparent quantum efficiency. The apparent quantum efficiency (AQE) of FOOPh-COF was 23.2% at 450 nm (Fig. 3e), confirming its excellent photocatalytic performance. Fig. 3f shows that the photocatalytic performance of FOOPh-COF is

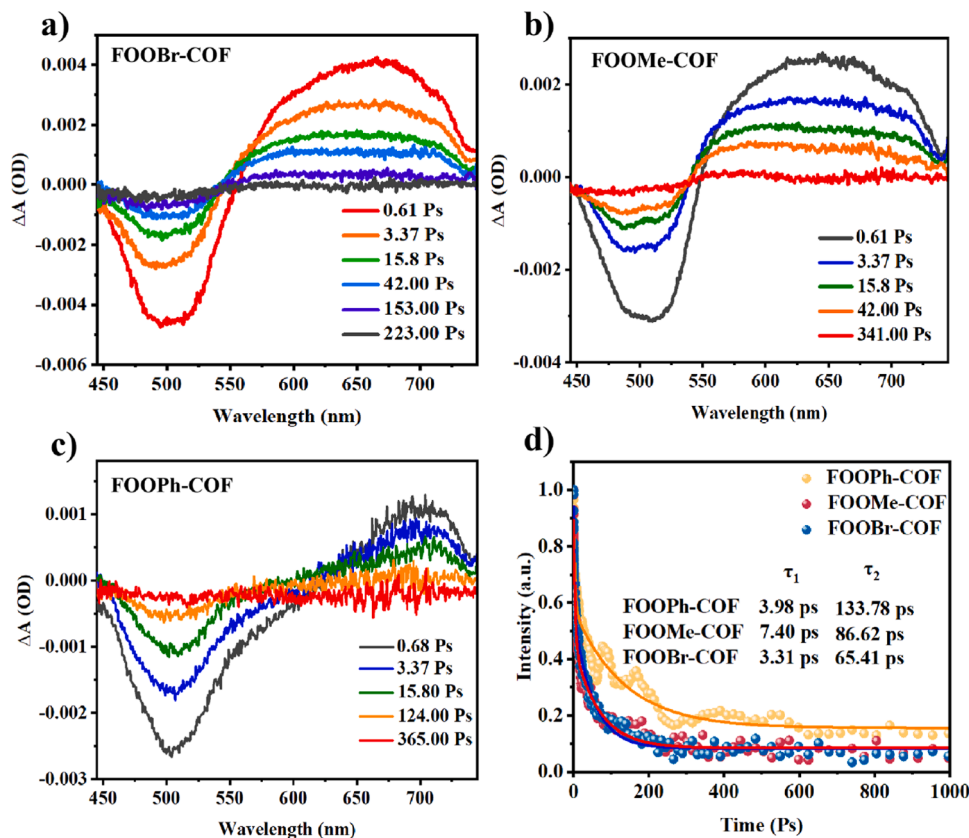


Fig. 4. Transient absorption spectroscopy testing. Fs-TA spectra: Excitation spectrum at 400 nm of a) FOOBr-COF. b) FOOMe-COF. c) FOOPh-COF. d) The decay kinetics were monitored at 675 nm of FOOBr-COF, FOOMe-COF and FOOPh-COF.

significantly superior to those of other reported COF-based photocatalysts. It is worth noting that even after undergoing standard conditions of photocatalytic testing, the skeleton structure of FOOPh-COF remains unchanged, further confirming its high stability (Figure S13-S16). Additionally, to evaluate its application potential, we conducted experiments with FOOPh-COF under natural sunlight illumination, measuring the real-time light intensity of 485 w/m^2 with a radiometer. The catalyst still exhibited excellent hydrogen evolution performance, generating obvious hydrogen bubbles (Figure S17). The indoor drainage and gas collection photocatalytic test also demonstrated the potential application of FOOPh-COF (Figure S18).

Electrochemical testing was employed to validate further the significant impact of different functional group modifications on the photocatalytic performance of fluorenone-based COFs. In electrochemical impedance spectroscopy (EIS) [48], it is observed that the FOOPh-COF exhibits the weakest charge transfer impedance (Figure S19)[49] and the strongest photocurrent (Figure S20)[50,51]. These results confirm the excellent semiconductor properties of FOOPh-COF. Furthermore, after light irradiation, FOOPh-COF generates higher signal peaks corresponding to higher photogenerated electron concentrations (Figure S21).

3.3. Photocatalytic mechanism analysis

To further observe the differences in photoelectron separation and transfer for three fluorenone-based COFs, femtosecond time-resolved transient absorption spectroscopy (fs-TAS) measurements were conducted to evaluate the real-time relaxation kinetics of photogenerated carriers[52]. A pump-probe configuration was utilized, with a 440 nm pump and a white light probe (440–700 nm), to monitor the dynamics of photogenerated electrons. All samples exhibit negative bands at 450–550 nm, confirming the ground state bleach (GSB) (Fig. 4a, b, c).

Correspondingly, a positive signal appears at 550–750 nm, indicating excited state absorption (ESA). This phase corresponds to the relaxation process of the excited electrons to the bottom of the CB. The holes remain in the VB after exciting the electrons from the VB to the CB. Understanding the dynamics of photogenerated electrons in the excited state absorption process is crucial for uncovering the key steps in the photocatalytic process[52]. The absorption peak at near 675 nm was analyzed. The highest absorption intensity was observed at 0.61 ps for FOOBr-COF and FOOMe-COF. In contrast, FOOPh-COF was observed at 0.68 ps. This indicates that there is not much difference in the photoexcitation stage of fluorenone-based COF modified by different functional groups. However, a significant distinction is observed in the decay stage of the peak at 675 nm, with FOOBr-COF decaying the fastest at 223.00 ps, followed by FOOMe-COF (341.00 ps) and FOOPh-COF decaying the slowest at 365.00 ps. This strongly indicates that the phenyl-modified FOOPh-COF can significantly inhibit the recombination of electrons and holes, extending the carrier lifetime[53]. Additionally, the decay processes of three COFs were fitted using a double exponential function. τ_1 and τ_2 represent electron capture and effective exciton dissociation, respectively (Fig. 4d). When Br is introduced into the fluorenone structure, FOOBr-COF shows the shortest electron capture and the worst exciton dissociation ($\tau_1 = 3.31 \text{ ps}$, $\tau_2 = 65.41 \text{ ps}$). When methyl groups are modified in the structure of fluorenone, electron capture, and effective exciton dissociation are significantly improved ($\tau_1 = 7.40 \text{ ps}$, $\tau_2 = 86.62 \text{ ps}$). When using phenyl to modify the structure of fluorenone, the inhibitory ability for carrier recombination reaches its maximum ($\tau_1 = 3.98 \text{ ps}$, $\tau_2 = 133.78 \text{ ps}$), corresponding to the maximum electron capture and exciton dissociation ability[54,55].

The molecular structure optimized by Density functional theory (DFT) can provide a more intuitive reflection of the local polarization and charge separation behavior of COF's structure[56]. The electrostatic

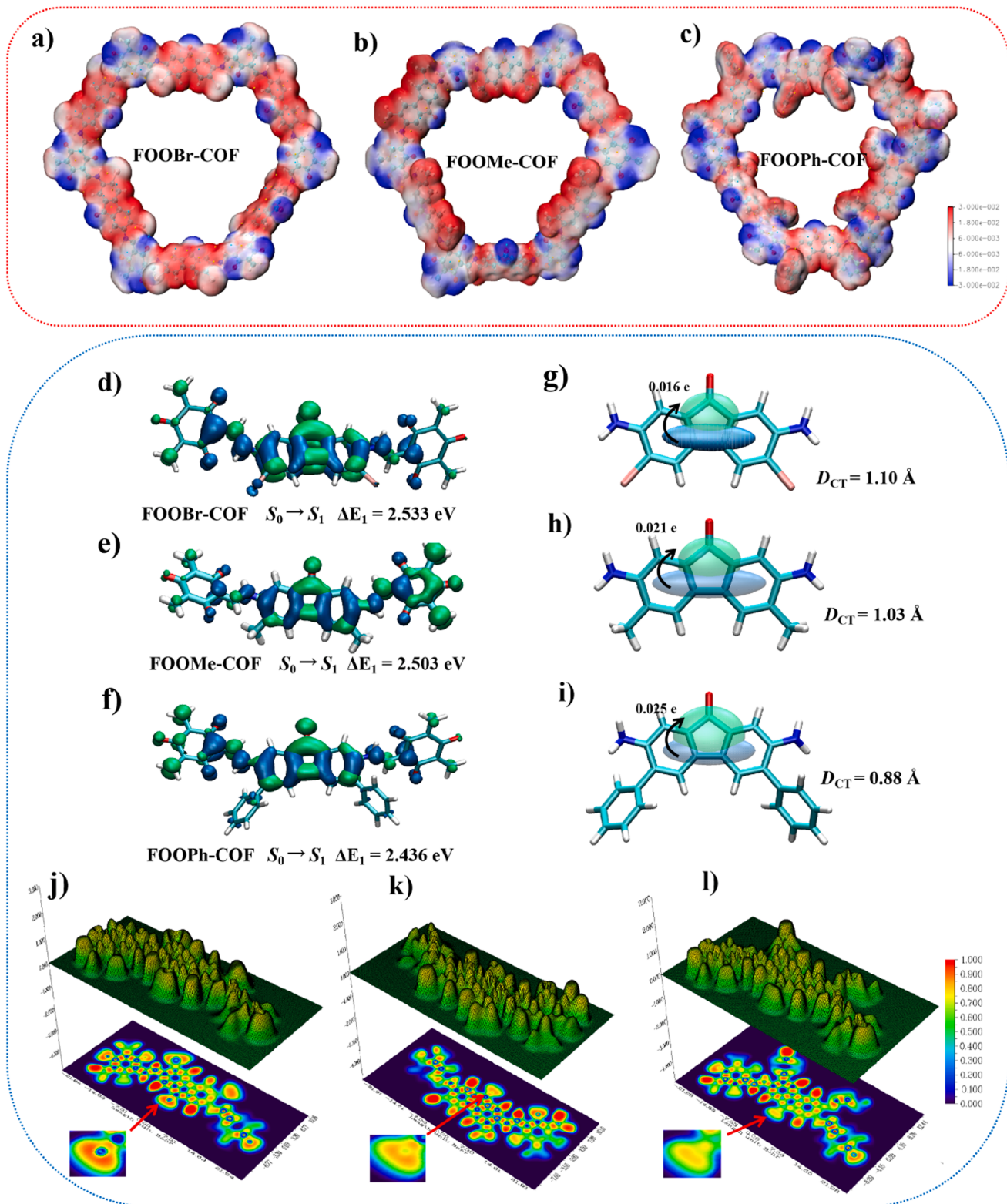


Fig. 5. Theoretical calculation and analysis. The electrostatic potential of a) FOOBr-COF, b) FOOMe-COF, and c) FOOPh-COF. Electron-hole distribution of local structures of d) FOOBr-COF, e) FOOMe-COF and f) FOOPh-COF in an Excited state (Green represents electrons, blue represents holes, and the isosurface is 0.002 a.u.). Computed charge density difference between the ground and the excited states of the g) FOOBr, h) FOOMe and i) FOOPh at an isovalue of 0.002 a.u. (The green and blue represent the increase and decrease in electron density, respectively. Quantitative charge-transfer analysis is based on the atomic dipole corrected Hirshfeld (ADCH) atomic charges. D_{CT} represents the distance between the barycenter of the density increment and depletion regions upon electronic excitation.) Topographic map and projection map of the electron localization function of the local structural plane of j) FOOBr-COF, k) FOOMe-COF, l) FOOPh-COF (at an isovalue of 0.002 a.u.).

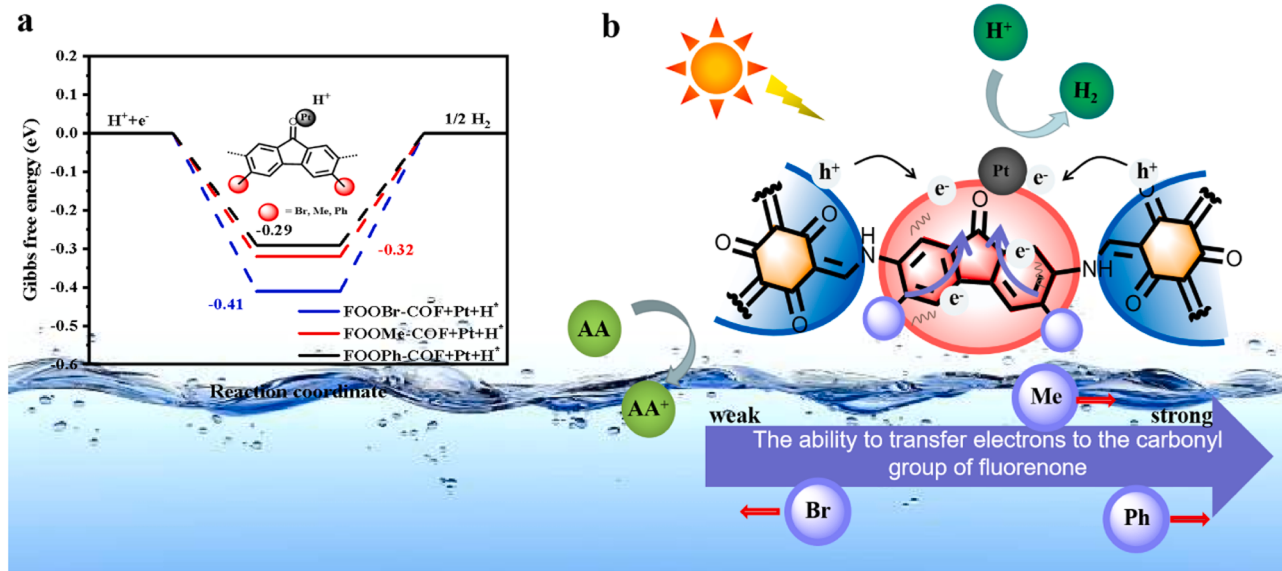


Fig. 6. a) Simulation of H* adsorption on Pt-loaded carbonyl sites in three fluorenone-based COFs (FOOX-COFs) structures. b) photocatalytic hydrogen evolution mechanism diagrams under standard conditions.

potential (ESP) analysis in three types of COFs reveals that the negative potential is predominantly found in the carbonyl region of the fluorenone structure (Fig. 5a-c). After resonance structural changes, the carbonyl group in the cyclohexane trione structure exhibits a negative potential distribution. However, due to the electron-rich effect of the benzene ring structure in the fluorenone structure, the amounts of electrons in the carbonyl group in the fluorenone structure are significantly higher than those in the cyclohexane trione structure. The electron density of the fluorenone's carbonyl group in FOOPh-COF modified with a benzene ring is higher than those in FOOMe-COF and FOOBr-COF. Due to the electron-pulling effect of bromine, the carbonyl group in the fluorenone structure of FOOBr-COF has the lowest electron content. In addition, their LUMO-HOMO distribution indicates that the most significant contribution to LUMO among the three types of COFs is the C=O of functionalized fluorenone. The HOMO distribution in the entire structure of FOOPh-COF modified with benzene rings is more delocalized (Figure S22-24). In addition, the exciton binding energy of three COFs was measured by temperature-dependent photoluminescence spectroscopy (PL) (Figure S25-27)[46,57,58]. Their PL intensity gradually decreases as the temperature increases from 80 to 230 K, corresponding to a thermally activated non-radiative recombination process. Subsequently, by fitting these data, it was found that the E_b (28.3 meV) of FOOPh-COF was lower than that of FOOMe-COF (32.0 meV) and FOOBr-COF (43.4 meV). The above results show that the electron density of the carbonyl group in the fluorenone structure can be significantly increased by grafting the electron-donating functional groups. Especially, the exciton binding energy of the FOOPh-COF can be significantly reduced after the modification with phenyl groups. This phenomenon can be attributed to the acceleration of charge transfer by the π electronic system, which enhances the photocatalytic performance.

To further investigate the specific effects of different functional group modifications on the carbonyl localized electrons in the structure of fluorenone, the study was conducted with the TD-DFT calculation to specify the distribution of electrons and holes in dissolution models [59]. Fig. 5d-f and S28-30 display the difference in the wavefunctions before and after vertical exclusion on the model, in which the green region is mainly located at the carbonyl of fluorenone signatures of the photo-induced electron accumulation, while the blue region is located at the biphenyl moiety of fluorenone, thereby well illustrating the photo-induced electron depletion. Based on the inter-fragment charge

transfer (IFCT) method, to avoid spatial asymmetry caused by large fragments, the value of rearranged electrons between three functionalized fluorenone fragments was calculated in the Hirshfeld partition to quantify the transferred charges (Fig. 5j-i) [60,61]. FOOPh has the shortest DCT value (0.88 Å) and the highest transfer electron quantity (0.025 e). The charge transfer distance and amount of FOOMe are 1.03 Å and 0.021 e, respectively. Due to the electron-pulling properties of Br atoms, the charge transfer of FOOBr is extended to 1.10 Å and the charge transfer amount decreases to 0.016 e. Therefore, FOOPh is most conducive to the photogenerated electron dynamics behavior in the excited state, and the corresponding COF has the best photocatalytic performance. The electronic localization functions of three COF structural fragments in the excited state were further investigated to reflect the electronic dynamics behavior inside the structure. This work uses the wave function files of three COF's structural fragments to obtain their electronic localization functions' topographic maps and projection maps. Figs. 5j, k, and l show a significant difference in the electronic localization function (ELF) of the carbonyl moiety of fluorenone after modification with functional groups. The ELF of carbonyl groups in the local fluorone structures of FOOBr-COF, FOOMe-COF, and FOOPh-COF are approximately 0.9, 0.8, and 0.7, respectively. The ELF index is used to evaluate the strength of electron localization within the structure. This indicates that the phenyl-modified fluorone structure enhances the electron-rich interaction of carbonyl groups and makes the carbonyl structure more delocalized locally, which is more conducive to the migration and transmission of photogenerated electrons.

The hydrogen evolution pathways of fluorenone carbonyl structures in three types of COFs were investigated using density functional theory (DFT) calculations. The Gibbs free energy changes (ΔG) of adsorbed hydrogen protons in the three COFs after Pt loading were evaluated (Fig. 6a). The results revealed that the hydrogen proton adsorption-free energies for three COFs were -0.41 (FOOBr-COF), -0.32 (FOOMe-COF), and -0.29 (FOOPh-COF) eV, respectively. Under the same conditions, the hydrogen proton adsorption-free energy of FOO-COF without functional group modification is -0.38 eV [38]. These findings further support the effectiveness of incorporating electron-donating functional groups to modify the local structure of fluorenone-based COFs in photocatalytic reactions (Fig. 6b).

4. Conclusion

In brief, three different functional group-modified fluorenone-based COFs were successfully designed and synthesized in this study. The aim is to directly regulate the carrier transport behavior of electron-rich active centers by modifying the acceptor module structure of the COFs. As a result, all COFs demonstrate excellent rates of photocatalytic hydrogen evolution. The FOOPh-COF, modified with phenyl functional groups, exhibits the highest activity at $228.5 \text{ mmol g}^{-1} \text{ h}^{-1}$ rate under visible light irradiation, 11.8 times higher than the rate of the FOOBr-COF modified with Br functional groups. The enhancement in photocatalytic activity is attributed to the introduction of electron-donating functional groups, particularly the benzene rings, which effectively shortens the carrier migration distance, facilitates electron delocalization in the carbonyl structures of fluorenone, increases the carrier migration rate, prolongs the carrier lifetime, and lowers the energy barrier for hydrogen proton adsorption. This makes the photocatalytic hydrogen evolution reaction more favorable. This study expands the new modification strategies of D-A-COFs in photocatalysis. It lays a solid foundation for precisely designing and synthesizing COF-based semiconductors with electron-rich active structures.

CRediT authorship contribution statement

Liang Guijie: Investigation, Data curation. **Kang Mengmeng:** Investigation. **Huang Can:** Investigation, Data curation. **Zhang Peng:** Writing – review & editing. **Li Xin:** Writing – review & editing, Funding acquisition, Data curation, Conceptualization. **Hao Lei:** Writing – original draft, Investigation, Formal analysis, Data curation, Conceptualization. **Shen Rongchen:** Formal analysis, Data curation.

Declaration of Competing Interest

The authors declare that they have no known competing financial interests or personal relationships that could have appeared to influence the work reported in this paper.

Data Availability

Data will be made available on request.

Acknowledgements

X.L. thanks National Natural Science Foundation of China (22378148, 21975084) and Natural Science Foundation of Guangdong Province (2021A1515010075) for their support.

Appendix A. Supporting information

Supplementary data associated with this article can be found in the online version at [doi:10.1016/j.apcatb.2024.123837](https://doi.org/10.1016/j.apcatb.2024.123837).

References

- [1] C. Liu, Q.F. Zhang, Z.G. Zou, J. Mater. Sci. Technol. 139 (2023) 167–188.
- [2] B.B. Zhao, W. Zhong, F. Chen, P. Wang, C.B. Bie, H.G. Yu, Chin. J. Catal. 52 (2023) 127–143.
- [3] S. Xiong, R.D. Tang, D.X. Gong, Y.C. Deng, J.F. Zheng, L. Li, Z.P. Zhou, L.H. Yang, L. Su, Chin. J. Catal. 43 (2022) 1719–1748.
- [4] Z.L. Li, T.C. Li, J.M. Miao, C.X. Zhao, Y. Jing, F.Y. Han, K. Zhang, X.F. Yang, Sci. China-Mater. 66 (2023) 2290–2298.
- [5] T. Li, N. Tsubaki, Z.L. Jin, J. Mater. Sci. Technol. 169 (2024) 82–104.
- [6] H. Yang, K. Dai, J.F. Zhang, G. Dawson, Chin. J. Catal. 43 (2022) 2111–2140.
- [7] Y.Q. Xing, S.Y. Liu, Chin. J. Struc. Chem. 41 (2022) 2209056–2209068.
- [8] Y.J. Ren, Y.F. Li, G.X. Pan, N. Wang, Y. Xing, Z.Y. Zhang, J. Mater. Sci. Technol. 171 (2024) 162–184.
- [9] Y.F. Li, Z.L. Xia, Q. Yang, L.X. Wang, Y. Xing, J. Mater. Sci. Technol. 125 (2022) 128–144.
- [10] J.N. Lu, S.A. Gu, H.D. Li, Y.A. Wang, M. Guo, G.W. Zhou, J. Mater. Sci. Technol. 160 (2023) 214–239.
- [11] C. Wu, K.L. Lv, X. Li, Q. Li, Chin. J. Catal. 54 (2023) 137–160.
- [12] H. Zhao, Q.Y. Mao, L. Jian, Y.M. Dong, Y.F. Zhu, Chin. J. Catal. 43 (2022) 1774–1804.
- [13] T. He, Y. Zhao, Angew. Chem. Int. Ed. 62 (2023) e202303086.
- [14] H. Chen, H.S. Jena, X. Feng, K. Leus, P. Van Der Voort, Angew. Chem. Int. Ed. 61 (2022) e202204938.
- [15] S. Karak, K. Dey, R. Banerjee, Adv. Mater. 34 (2022) e2202751.
- [16] H. Zhao, L. Wang, G. Liu, Y. Liu, S. Zhang, L. Wang, X. Zheng, L. Zhou, J. Gao, J. Shi, Y. Jiang, ACS Catal. 13 (2023) 6619–6629.
- [17] H. Wang, H. Wang, Z. Wang, L. Tang, G. Zeng, P. Xu, M. Chen, T. Xiong, C. Zhou, X. Li, D. Huang, Y. Zhu, Z. Wang, J. Tang, Chem. Soc. Rev. 49 (2020) 4135–4165.
- [18] H. Lin, Y. Liu, Z. Wang, L. Ling, H. Huang, Q. Li, L. Cheng, Y. Li, J. Zhou, K. Wu, J. Zhang, T. Zhou, Angew. Chem. Int. Ed. 61 (2022) e202214142.
- [19] Z. Liu, X. Yang, Z. Yang, X. Su, Z. Xie, W. Chen, W. Zhang, L. Chen, Appl. Catal. B 312 (2022) 121406.
- [20] X. Ren, X. Wang, W. Song, F. Bai, Y. Li, Nanoscale 15 (2023) 4762–4771.
- [21] H. He, R. Shen, P. Zhang, G. Liang, X. Li, J. Mater. Chem. A 12 (2024) 227–232.
- [22] R. Shen, X. Li, C. Qin, P. Zhang, X. Li, Adv. Energy Mater. 13 (2023) 2203695.
- [23] R. Shen, N. Li, C. Qin, X. Li, P. Zhang, X. Li, J. Tang, Adv. Funct. Mater. 33 (2023) 2301463.
- [24] C. Li, J. Liu, H. Li, K. Wu, J. Wang, Q. Yang, Nat. Commun. 13 (2022) 2357.
- [25] S.H. Wu, C. Li, Y. Wang, Y. Zhuang, Y. Pan, N. Wen, S. Wang, Z.Z. Zhang, Z.X. Ding, R.S. Yuan, W.Y. Dai, X.Z. Fu, J.L. Long, Angew. Chem. Int. Ed. 62 (2023) e202309026.
- [26] K. Huang, J. Bai, R. Shen, X. Li, C. Qin, P. Zhang, X. Li, Adv. Funct. Mater. 33 (2023) 2307300.
- [27] M. Hao, Y. Xie, X. Liu, Z. Chen, H. Yang, G.I.N. Waterhouse, S. Ma, X. Wang, JACS Au 3 (2023) 239–251.
- [28] H. Yang, M. Hao, Y. Xie, X. Liu, Y. Liu, Z. Chen, X. Wang, G.I.N. Waterhouse, S. Ma, Angew. Chem. Int. Ed. 62 (2023) e202303129.
- [29] R. Luo, H. Lv, Q. Liao, N. Wang, J. Yang, Y. Li, K. Xi, X. Wu, H. Ju, J. Lei, Nat. Commun. 12 (2021) 6808.
- [30] H. Zhang, Z. Lin, P. Kidkhunthod, J. Guo, Angew. Chem. Int. Ed. 62 (2023) e202217527.
- [31] F.D. Wang, L.J. Yang, X.X. Wang, Y. Rong, L.B. Yang, C.X. Zhang, F.Y. Yan, Q. L. Wang, Small 19 (2023) e2207421.
- [32] C. Shu, C. Han, X. Yang, C. Zhang, Y. Chen, S. Ren, F. Wang, F. Huang, J.X. Jiang, Adv. Mater. 33 (2021) 2008498.
- [33] W. Chen, L. Wang, D. Mo, F. He, Z. Wen, X. Wu, H. Xu, L. Chen, Angew. Chem. Int. Ed. 59 (2020) 16902–16909.
- [34] W. Li, X. Huang, T. Zeng, Y.A. Liu, W. Hu, H. Yang, Y.B. Zhang, K. Wen, Angew. Chem. Int. Ed. 60 (2021) 1869–1874.
- [35] C. Shu, C. Han, X. Yang, C. Zhang, Y. Chen, S. Ren, F. Wang, F. Huang, J.X. Jiang, Adv. Mater. 33 (2021) 2008498.
- [36] F. Zhang, X. Dong, Y. Wang, X. Lang, Small 19 (2023) e2302456.
- [37] L. Hao, R. Shen, S. Chen, W. Bi, L. Wang, G. Liang, P. Zhang, X. Li, J. Mater. Chem. A 10 (2022) 24064–24072.
- [38] L. Hao, R. Shen, C. Huang, Z. Liang, N. Li, P. Zhang, X. Li, C. Qin, X. Li, Appl. Catal. B 330 (2023) 122581.
- [39] A. Putta Rangappa, D. Praveen Kumar, K.H. Do, J. Wang, Y. Zhang, T.K. Kim, Adv. Sci. (Weinh.) 10 (2023) e2300073.
- [40] S. Bao, Q. Tan, S. Wang, J. Guo, K. Lv, S.A.C. Carabineiro, L. Wen, Appl. Catal. B 330 (2023) 122624.
- [41] Y. Yang, X. Chu, H.Y. Zhang, R. Zhang, Y.H. Liu, F.M. Zhang, M. Lu, Z.D. Yang, Y. Q. Lan, Nat. Commun. 14 (2023) 593.
- [42] Z. Wang, X. Yang, T. Yang, Y. Zhao, F. Wang, Y. Chen, J.H. Zeng, C. Yan, F. Huang, J.-X. Jiang, ACS Catal. 8 (2018) 8590–8596.
- [43] F.M. Zhang, J.L. Sheng, Z.D. Yang, X.J. Sun, H.L. Tang, M. Lu, H. Dong, F.C. Shen, J. Liu, Y.Q. Lan, Angew. Chem. Int. Ed. 57 (2018) 12106–12110.
- [44] K. Xiong, Y. Wang, F. Zhang, X. Li, X. Lang, Appl. Catal. B: Environ. 322 (2023) 122135.
- [45] D. Chen, W. Chen, Y. Wu, L. Wang, X. Wu, H. Xu, L. Chen, Angew. Chem. Int. Ed. 62 (2023) e202217479.
- [46] J. Xu, C. Yang, S. Bi, W. Wang, Y. He, D. Wu, Q. Liang, X. Wang, F. Zhang, Angew. Chem. Int. Ed. 59 (2020) 23845–23853.
- [47] R. Shen, L. Zhang, N. Li, Z. Lou, T. Ma, P. Zhang, Y. Li, X. Li, ACS Catal. 13 (2022) 9994–10003.
- [48] W. Dong, Z. Qin, K. Wang, Y. Xiao, X. Liu, S. Ren, L. Li, Angew. Chem. Int. Ed. 62 (2023) e202216073.
- [49] Y. Zhao, P.V. Kumar, X. Tan, X. Lu, X. Zhu, J. Jiang, J. Pan, S. Xi, H.Y. Yang, Z. Ma, T. Wan, D. Chu, W. Jiang, S.C. Smith, R. Amal, Z. Han, X. Lu, Nat. Commun. 13 (2022) 2430.
- [50] J.N. Chang, Q. Li, J.W. Shi, M. Zhang, L. Zhang, S. Li, Y. Chen, S.L. Li, Y.Q. Lan, Angew. Chem. Int. Ed. 62 (2023) e202218868.
- [51] J. Zhang, C.Y. Toe, P. Kumar, J. Scott, R. Amal, Appl. Catal. B 333 (2023) 122765.
- [52] R. Shen, G. Liang, L. Hao, P. Zhang, X. Li, Adv. Mater. 35 (2023) 2303649.
- [53] C. Mo, M. Yang, F. Sun, J. Jian, L. Zhong, Z. Fang, J. Feng, D. Yu, Adv. Sci. 7 (2020) 1902988.
- [54] D.H.K. Murthy, H. Matsuzaki, Z. Wang, Y. Suzuki, T. Hisatomi, K. Seki, Y. Inoue, K. Domen, A. Furube, Chem. Sci. 10 (2019) 5353–5362.
- [55] J. Xue, J. Bao, Surf. Interfaces 25 (2021) 101265.
- [56] H. Ben, G. Yan, H. Liu, C. Ling, Y. Fan, X. Zhang, Adv. Funct. Mater. 32 (2022) 2104519.
- [57] M. Melchionna, P. Fornasiero, ACS Catal. 10 (2020) 5493–5501.

- [58] X. Wang, L. Chen, S.Y. Chong, M.A. Little, Y. Wu, W.H. Zhu, R. Clowes, Y. Yan, M. A. Zwijnenburg, R.S. Sprick, A.I. Cooper, *Nat. Chem.* 10 (2018) 1180–1189.
- [59] T. Lu, F. Chen, *J. Comput. Chem.* 33 (2012) 580–592.
- [60] Z. Gao, S. Chen, Y. Bai, M. Wang, X. Liu, W. Yang, W. Li, X. Ding, J. Yao, *Phys. Chem. Chem. Phys.* 23 (2021) 11548–11556.
- [61] Y. Qian, Y. Han, X. Zhang, G. Yang, G. Zhang, H.L. Jiang, *Nat. Commun.* 14 (2023) 3083.